A refined ephemeris and phase resolved X-ray spectroscopy of the Geminga pulsar

M. S. Jackson and J. P. Halpern

Department of Astronomy, Columbia University, New York, NY, 10025-6601

ABSTRACT

We present a refined phase-connected post-glitch ephemeris for the Geminga pulsar that is a good fit to all the post-glitch data from EGRET, *ASCA*, and *XMM-Newton*. We also present the results of phase-resolved spectroscopy of two *XMM-Newton* X-ray observations of the Geminga pulsar obtained in 2002 and 2004. An investigation is made into a previously claimed existence of a small hot spot on the neutron star surface. We conclude that that interpretation was more likely an artifact of an overly restrictive assumption used to fit the phase-resolved spectra, namely, that the spectral index of the non-thermal component is constant. When we allow the spectral index to vary as a function of rotation phase, we find systematic variations in spectral index, and such fits do not require an additional, hot blackbody component.

Subject headings: pulsars: individual (Geminga)— stars: neutron — X-rays: stars

1. Introduction

Since its discovery in 1972 (Fichtel et al. 1975; Thompson et al. 1977), the Geminga pulsar has been determined to be a relatively old radio-quiet pulsar with a period of 237 ms, which modulates in X-rays (Halpern & Holt 1992), γ-rays (Bertch et al. 1992), and at optical wavelengths (Shearer et al. 1998) (see Bignami & Caraveo (1996) for a review). A glitch occurred in late 1996 and the post-glitch ephemeris was calculated from EGRET data (Jackson et al. 2002). The latest *XMM-Newton* observations have been used to further refine the ephemeris. The method and resulting new ephemeris are presented here.

Unlike the observed hard X-ray and γ-ray emission, which is thought to arise in the magnetosphere, the soft X-ray and ultraviolet radiation is thermal in nature and is produced at the neutron star surface itself. As a neutron star of Geminga's age cools, the interior heat travels preferentially along the magnetic field lines, producing relatively warm areas at the

poles. As the star rotates, the amount of surface area of these areas exposed to the observer changes, giving rise to pulsed emission. The shape of the thermal light curves is strongly determined by the angle between the magnetic and rotation axes, and by the position of the observer with respect to the rotation axis.

The 2002 *XMM-Newton* observation allowed for the first time the opportunity to perform statistically significant phase-resolved spectroscopy on Geminga data. Prior to this, the *ASCA* data provided for dividing the spectra into two parts based on the phase, and the difference in the fitted parameters was only marginally significant (Jackson et al. 2002). With phase-resolved spectroscopy it is possible to determine the changes in the individual spectral components as the pulsar rotates, to give a more thorough picture of the various emission regions.

It has recently been proposed (Caraveo et al. 2004; De Luca et al. 2004) that the pulsed thermal emission from Geminga and other pulsars is composed of a power law component and two blackbody components, one arising from a large warm area on the neutron star surface and the other from a hot spot located at the polar cap. Those authors performed fits on the phase-resolved spectra by freezing the hydrogen column density, warm and hot blackbody temperatures, and photon index at the values obtained from a fit to the entire spectrum. It is expected that the column density and temperatures would remain constant, considering the physical meaning of those parameters. However, there is no reason that the photon index, which is a property of the emission from the magnetosphere, would remain constant with rotation phase. The blackbody components represent thermal emission from the surface of the pulsar, but the power-law component is only a parameterization of the magnetospheric emission, and it is used as a convenience for fitting the pulsar spectrum in a particular energy range, without a rigorous physical model to support its use.

For all three pulsars that were investigated in this manner (De Luca et al. 2004), the authors found a phase difference between the warm and hot emission, and in fact for the pulsar PSR0656+14 these two blackbody components are almost exactly out of phase with each other, meaning that the hot spot and warm region are not in the same location, leading to the question of whether there are two separate heating mechanisms at work, or whether the thermal conductivity on the surface does not behave as expected. Kargaltsev et al. (2005) bring into question the existence of the hot spot on Geminga because the radius for the hot spot (50 m) is much less than the expected size of the polar cap at the surface (300 m). However, those authors did not perform phase resolved spectroscopy and did not offer an alternative model or an explanation for the excess of counts above the model in some of the X-ray spectra. In their paper, an attempt is made to connect the spectrum among the visual, UV, and X-ray ranges. Additional observations would be required at the unmeasured

energy bands to discover the full spectral shape.

2. Observations and data preparation

A log of the observations used in this paper is given in Table 1. A long observation of Geminga was performed by *XMM-Newton* in 2002, and a shorter observation in April 2004, for the primary purpose of maintaining the phase-connected ephemeris. The shorter 2004 observation does not provide enough counts to use it exclusively in order to perform phase-resolved spectroscopy.

The X-ray data used in this paper are primarily the EPIC-pn data from the two *XMM-Newton* observations. The data from the EPIC-MOS instruments do not have sufficient timing resolution for phase resolved spectroscopy. MOS spectra can be used to fit the entire spectrum to make sure the fitted parameters are reasonable.

The EGRET and *ASCA* GIS data used are as described in Jackson et al. (2002), and were extracted and prepared in the same manner as previously published. The resulting data are in the form of barycenter-corrected event files, containing positions and arrival times of detected photons.

The latest version of the Science Analysis System (SAS) package (version 6.1) for *XMM-Newton* data analysis was used to process the *XMM-Newton* data into event files. The SAS package contains a useful ftool called *barycen* that performs the barycentric correction on *XMM-Newton* EPIC-pn data. It uses many of the housekeeping files that are included with the data, for spacecraft position, etc. The timing resolution of the pn instrument in small window mode is 5.7 ms, which is sufficient for timing analysis of Geminga.

The data for all *XMM-Newton* pn observations were extracted from a circle of radius $29''$, with a background circle with the same radius, offset from the source, as shown in Figure 1. These regions were chosen to maximize the signal to noise ratio. Events were selected for both spectra and light curves based on the FLAG parameter set to zero, and the PATTERN parameter of 4 or less. There was no evidence for pileup in either observation.

For the phase-resolved spectra an additional criterion that the chosen events fall into phase bins of 0.1 cycles is used, and one spectrum is produced for each of ten equally spaced phase ranges, with zero phase corresponding to T_0 of the ephemeris given in Table 2. The SAS program *especget* extracts source and background spectra and produces arf and rmf response files. The spectra were binned with a minimum of 40 counts in each bin for the whole spectrum and 25 counts for the phase-resolved spectra.

2.1. XMM Timing errors

It should be noted that the 2002 *XMM-Newton* observation was found to have a timing jump of 7 seconds for approximately one-third of the observing time. This arose from three of the bit counters getting flipped. It was corrected when the timing counter reached its maximum and was reset. Before the latest version of SAS (6.1) was released, it was necessary to correct the shifted times by hand, and this greatly improved the appearance of the light curves. Version 6.1 of SAS now corrects for this error, though it is as yet uncertain if it will correct for all such errors in future observations.

It is suspected that the timing errors in *XMM-Newton* pn data occur between the times when the timing counter is reset, which happens at the beginning of every observation and once or more during long observations. It was believed that it was not possible for there to be a timing error in a single short observation, which does not have enough duration for the timing counter to have reached its maximum and reset.

Figure 2 shows the phase residuals for all X-ray and EGRET observations of Geminga using the preglitch ephemeris given in Mattox, Halpern, & Caraveo (1998). The phase residual of the 2004 *XMM-Newton* observation lies at a phase that is approximately 0.2 (or 0.8) away from the ephemeris calculated in this paper from the EGRET points. This indicates either that a second (comparatively larger than that of 1996) glitch occurred between the epochs of the 2002 and 2004 *XMM-Newton* observations, or that there was a timing error in the 2004 observation that was not corrected by the software. Future observations will determine which of these possible explanations is correct.

If the phase jump resulted from a glitch, an estimate can be made of the glitch size. With only one post-glitch point there is no way of estimating the epoch of the glitch, but assuming that the possible glitch occurred shortly after the 2002 observation, the value of $\Delta f/f$ is estimated to be 3×10^{-9}, which is 5 times the size of the 1996 glitch. That value is a lower limit for the glitch magnitude. If the possible glitch occurred later, or if the phase residual is, say, –1.8 instead of –0.8, that would result in a larger calculated value of the glitch.

If the phase shift resulted from a timing error, the most likely correction is to subtract 1 second from each arrival time. Out of all possible corrections, that of –1 second yielded a result that best lines up with the calculated ephemeris. The possible corrected point is indicated by the open circle beneath the 2004 point in Figure 2.

Whether a second glitch did occur will be determined from the next Geminga observation. However, as this data set was only used to check the new ephemeris and not to calculate it, the timing error (if any) is somewhat unimportant to the results of this paper,

for timing up to epoch of the 2002 *XMM-Newton* observation, or for the spectroscopy. This timing issue does not affect the results of the phase resolved spectroscopy, as the data were lined up in phase with the 2002 observation before the spectra were extracted.

3. Determination of the Post-Glitch Ephemeris

The EGRET observations fortunately provide data for a timeline of nearly 1400 days after the glitch, which means that from the EGRET data alone, the post-glitch ephemeris parameters can be determined. All of the EGRET photon arrival times after the 9th EGRET observation (approximately when the glitch occurred) were used to find f and $\dot{f}$.

An iterative search has been performed for the f and $\dot{f}$ parameters, by using Z_n^2 and folding techniques. The search alternates between finding the best value for f and $\dot{f}$, while holding the other fixed. The value of Z_2^2 is determined at each f or $\dot{f}$, and light curves are made with 12 and 20 bins, from which χ^2 is determined for each. The value of the varying parameter that gives the maximum Z_2^2 and χ^2 is the best, and is then used for the next iteration.

To establish initial f and $\dot{f}$, the first and last post-glitch EGRET observations are used (the 10th and 14th observations in Table 1), and a frequency is determined for each with $\dot{f}$ set at zero. From these quantities and the amount of elapsed time between the two observations, a value of $\dot{f}$ is calculated. This preliminary $\dot{f}$ is used in a search for f, using all five post-glitch EGRET observations (10–14 in Table 1), centered at the preliminary frequency as determined from the first post-glitch observation. Given this newly determined frequency, a search is then done for $\dot{f}$, centered at its preliminary value. This process is continued iteratively until the parameters don't change from one iteration to the next. These parameters are then checked with the XMM data.

The uncertainties in the f and $\dot{f}$ parameters estimated from this method are given by a reduction in the statistic of approximately $1\,\sigma$, based on the number of degrees of freedom implicit in the statistic. The uncertainty values from the Z_2^2 and folding χ^2 statistics are usually in good agreement.

The resulting post-glitch ephemeris, with an epoch T_0 chosen so that the phase lines up with the previous ephemeris, is given in Table 2, and the summed EGRET light curve folded at the new ephemeris is shown in the bottom panel of Figure 3. The post-glitch EGRET observations show a much more consistent position of the peaks in phase, compared with one another and with the previous ephemeris. While it is not possible to determine the exact epoch of the glitch, the extrapolation of the post-glitch points in Figure 2 give a good

estimation. The glitch occurred at a time very soon after the 9th EGRET observation in late 1996. By adjusting the estimated glitch epoch, it is possible to determine the point at which the curve given by the new ephemeris lines up best with the post-glitch EGRET, *ASCA* and *XMM-Newton* points in Figure 2. This epoch was found to be MJD 50320.

3.1. Refining the ephemeris using *XMM-Newton* pn data

Given f and $\dot{f}$ parameters from the EGRET photon arrival times up to 2000, the newer XMM observations can be used to test the validity and continuity of these values. Whereas the absolute phases of the EGRET peaks can be determined by using a fit to Lorentzians as described in Jackson et al. (2002), it is not as straightforward to determine the absolute phases of the X-ray light curves. The phases of the X-ray peaks relative to the γ-ray peaks have been established with previous EGRET and ASCA data, so a similar comparison can be made between the EGRET peaks and XMM light curves from a more recent epoch. Figure 3 shows the 1994 and 1999 *ASCA* GIS, and 2002 and 2004 *XMM-Newton* pn light curves, along with the EGRET light curve. As can be seen from that Figure, the X-ray peaks line up with each other using the new ephemeris, and the large peak in the 0.7 – 2.0 keV X-ray light curves consistently occurs approximately 0.05 later in phase than the first EGRET peak.

To determine the phase difference between two X-ray observations, the light curves for an identical energy range are compared in a bin by bin fashion, and a χ^2 value is calculated. This is done while varying the phase of the second light curve between 0.00 and 0.99 in 0.01 increments. The calculated phase difference between the two data sets is given by the value that produces the smallest χ^2.

The uncertainty on the phase for a given X-ray observation is calculated by creating a template light curve, composed of the 2002 and 2004 *XMM-Newton* EPIC-pn observations, folded at an ephemeris determined by a method similar to that described in Section 5. This template light curve is compared to each of the X-ray light curves from the *ASCA* and *XMM-Newton* observations and is shifted away from its best value until the χ^2 value increases by 1σ. This gives the uncertainty for each of the labeled X-ray points shown in Figure 2. An example showing the template light curve compared with the 1994 *ASCA* GIS light curve is shown in Figure 4.

4. Timing Results

Figure 5 shows summed X-ray and γ-ray light curves from 0.1 keV – 7.0 keV, and above 100 MeV, folded at the post-glitch ephemeris, given in the second column of Table 2. These light curves can be compared with Figure 4 of Jackson et al. (2002).

It can be seen from Figure 2 that the Geminga ephemeris, consisting of 2 cubic segments covering 1973–1996 and 1996–2004 given in Table 2, is phase-connected and valid for the full specified epoch range. Apart from instances of timing noise, which manifest themselves as phase deviations from the solid line in Figure 2, the only confirmed glitch since 1973 occurred in late 1996. In this paper, the term "pre-glitch" refers to epochs before the 1996 glitch.

For the ephemeris search, the value of $\dddot{f}$ was assumed to be zero, as that parameter would not have significantly affected the fits, given the 1400 day timeline. Figure 2 indicates that when the $\dddot{f}$ parameter is zero, the ephemeris matches the data well, and the phase residuals for the 2002 *XMM-Newton* observation using the post-glitch ephemeris are consistent with zero, also indicating that the post-glitch ephemeris parameters, including the $\dddot{f}$ value, are valid up to at least 2002. Further *XMM-Newton* observations will allow for a determination of the ephemeris from X-ray data alone, using the method described in Section 5. This will assure that the ephemeris is consistent and phase-connected and will also determine whether a glitch occurred between the 2002 and 2004 *XMM-Newton* observations.

5. Spectral Analysis

The combined 2002 and 2004 *XMM-Newton* EPIC-pn full spectra, extracted as described in Section 2, were fitted between energies of 0.2 and 10.0 keV, to an absorbed power law and one or two blackbody components. The spectra showing the power law and blackbody components are given in Figure 6 and the fitted parameters are given in Table 3.

The values of the power law index are consistent with those from previous *ASCA* measurements (Jackson et al. 2002) and the previously published value from the 2002 *XMM-Newton* data (Caraveo et al. 2004), and between the 2002 *XMM-Newton* measurement alone and the combined 2002 and 2004 fit, but the addition of the hot blackbody component decreases the value of this parameter. The fitted temperature of the warm blackbody component is consistent with the *ROSAT* and *ASCA* values (Halpern & Wang 1997), and both warm and hot blackbody temperatures are consistent with the previously published values from the 2002 observation (Caraveo et al. 2004).

The poor response of the detector at low energies results in a large error bar on the

column density and the fit of that parameter is strongly coupled to the parameters of the warm blackbody component. However, the value is consistent among fits of one and two blackbody components to the 2002 observation alone and the combined 2002 and 2004 data, and larger than (but within uncertainty of) those that arose from fits performed on $ROSAT$ and combined $ROSAT$ and $ASCA$ data (Halpern & Wang 1997; Halpern & Ruderman 1993). It was noted at the time of those measurements that the $ROSAT$ PSPC entrance window was becoming progressively thinner, allowing more low energy photons to pass through and leading to a smaller and smaller measured column density. The true column density is therefore most likely greater than the 1.07×10^{20} cm^{-2} value from $ROSAT$ data or the 1.38×10^{20} cm^{-2} value from combined $ROSAT$ and $ASCA$ data given in Halpern & Wang (1997).

As is shown in Table 3, combining the 2004 spectrum with that of the 2002 observation has the effect of reducing the error bars on the parameters. Although the reduced χ^2 value increases slightly, the fit to the combined data results in parameters very consistent with those from the 2002 observation alone.

To fit the phase-resolved spectra using the one and two blackbody plus power law models, the column density was frozen at its fitted value from the fits to the entire spectrum. Data between 0.2 and 8.0 keV were used for these fits, as the statistics at greater energies are not sufficient to make reliable fits. For the first fits to the phase-resolved spectra, all parameters other than the column density were allowed to vary. Whereas Caraveo et al. (2004) noted that the photon index did not show significant variation over the rotation cycle, we observe significant variability of the photon index for fits of both one and two blackbody components, as shown in the 2 and 3 σ contours in Figure 7. Whereas it appears that the lower panel of Figure 7 shows that as few as two points differ from the mean value as well as any possible chosen photon index value by 3σ or more, this would occur with less than 0.1% probability if the photon index were in fact constant. Another fact supporting the reality of the variability of the spectral index is that the values trace out a loop in Figure 7 (both top and bottom panels). That is, not only do the values differ by a few σ, but they differ in a non-random order. This behavior must enhance the statistical significance of the variation, although it is not as easy to quantify.

We do confirm the result of Caraveo et al. (2004) that the blackbody temperatures are constant within uncertainty, as would be expected for rotating hot or warm spots, and thereafter these temperatures were frozen for the fits. The absorbed power law with a variable photon index plus one or two blackbody components with fixed temperatures are hereafter referred to as Models A & B. The resulting fitted parameters for both models (Models A & B) are given in Table 4, and the fitted phase resolved spectra and their ratio to the model are

shown in Figures 8 and 9. The values of the reduced χ^2 are not significantly decreased with the addition of the second blackbody component (Model B) and in some cases it actually increases (though the value of χ^2 does not increase), and most of the normalization values for the hot blackbody component are consistent with zero, considering the rather large error bars, so it is not clear that the hot blackbody component is present in the spectra at all, except in one or two phase bins where the value of the emitting radius exceeds its error bar.

As a test of the consistency between the results given here and the previously published results (Caraveo et al. 2004), the method used in that paper was employed here. For the fits to the phase resolved spectra, the two blackbody plus power law model was employed, with the power law index fixed at the value obtained for the full spectrum, and everything else the same as in Model B, i.e. the temperatures and column density frozen as well, leaving only the normalizations of the three components to vary. This model is hereafter referred to as Model C. The results are given in Table 4, and the parameters are similar to those in Caraveo et al. (2004), with the the hot blackbody component more significant than when the power law index was allowed to vary. The fitted phase resolved spectra and their ratio to the model (Model C) are shown in Figure 10.

From Figures 8, 9, and 10, it is clear that Models A, B, and C fit the data approximately equally well for each phase-resolved spectrum, especially at energies below 5 keV, and the unfitted features in some of the phase bins are apparent for all of the models. For example, for the 0.8–0.9 phase bin, there is a dip in the spectrum compared to the model at 0.5 keV, and for the 0.2–0.3 and 0.3–0.4 phase bins, there is a narrow hump between 0.3 and 0.4 keV. Since these features are apparent in both the 2002 and 2004 data sets, these are more likely actual spectral features that are not well-fit by the model being used, than remnants of poor statistics in the phase-resolved spectra. Clearly there is an as yet unexplained process that emits in X-rays, but it is not described by the models employed here, and it could have its origin either on the neutron star surface or in the magnetosphere.

The variation of the emitting radii of the blackbody components and power law intensity for the models are shown in Figure 11. The warm blackbody component is prominent at the lowest energies, and the power law component dominates at higher energies. When the power law index is fixed, the hot blackbody component modulates approximately with the power law component, and not with the warm blackbody component as would be expected from a model where the neutron star surface is heated from the interior along the field lines near the poles.

A possible explanation for the behavior of the spectral parameters in the fits, specifically the variation of the hot blackbody component in Model C, was tested by creating a fake spectrum for each of the 10 phase bins with the parameters given in the first column of

Table 4 (the power law plus single blackbody, Model A). Using these fake spectra as input, fits were made using a model containing a power law and two blackbody components, with temperatures and photon index fixed as they were for Model C. The resulting parameters are very similar to those obtained from fitting the real spectra to Model C. It is quite evident from the similarity between the parameters that the varying photon index in the true spectra produces an excess of residual counts in fits where the photon index is held fixed, and these excess counts can be fit by a second blackbody component. That does not mean the hot blackbody component is present in the spectra but it could be the result of erroneously freezing the photon index for the fits where it is clear from Figure 7 that it in fact varies at a > 99.9% confidence level.

6.   Results of Phase-resolved Spectroscopy

While there is some evidence for a variable hot blackbody component in the *XMM-Newton* Geminga phase resolved spectra when the photon index is held fixed, we find that the strength of the variation is not nearly as clear-cut as has been previously stated (Caraveo et al. 2004). The residuals from a single blackbody plus power law fit could arise from the magnetospheric emission not being accurately described by a power law. This argument is strengthened by the fact that the hot blackbody normalization for Model C closely matches the strength of the power law component in the light curves. The *XMM-Newton* data do not prove conclusively that there is a rotating hot spot on the neutron star surface, and it is more likely that the emission from the hot spot would have a low pulsed fraction, than that it completely disappears for 1/10 of the rotation. The two-blackbody fits to the fake spectra, which were made to conform to the fitted parameters of the single blackbody fits, result in parameters that closely match those from similar fits to the real data, and the apparent disappearance of the hot blackbody component for 1/10 of the phase was due to the fact that the correction to the fixed photon index model provided by the addition of the second blackbody was not necessary for that particular dataset.

The method used in this and previous papers, i.e. to fit the entire spectrum to a single power law and one or two blackbody components, and then to use some of the parameters for subsequent fits to the phase-resolved data, does not take into account the fact that the sum of power laws is not itself a power law. While it is unlikely that the magnetospheric emission is a power law, even over the limited 0.2–8 keV energy range for a fraction of the rotation, the full spectrum, which is a sum of the emission for the full period, is even less likely to be a power law. Unfortunately, the exposure times of the observations used for this paper were not sufficient to accumulate spectra that will answer the question of the exact

spectral shape of the phase-resolved spectra, but the data provide a much better picture of the variation of the spectrum over the rotation of the pulsar, and it can safely be concluded that both the magnetospheric and surface emission vary significantly.

It is not clear whether the non-thermal component of the X-ray spectrum of Geminga can be extrapolated to the ultraviolet and optical range, and it has already been established in previous work that the spectrum does not extrapolate to γ-ray energies (Jackson et al. 2002). The power law index in the X-ray regime is less uncertain with the new *XMM-Newton* observations, but it strongly depends on other parameters such as the column density and the strength and temperature of the warm and hot (if present) blackbody components. As previously stated, the non-thermal component of the spectrum is parameterized by a power law, but it is not certain that the spectrum is a power law or that it would continue with the same slope at all energies.

REFERENCES

Bertch, D. L., et al. 1992, Nature 357, 306

Bignami, G. F., & Caraveo, P. A. 1996, ARA&A 34, 331

Caraveo, P. A., Lattanzi, M. G., Massone, G., Mignani, R. P., Makarov, V.V., Perryman, M. A. C., & Bignami, G. F. 1998, A&A, 329, L1

Caraveo, P. A., De Luca, A., Mereghetti, S., Pellizzoni, A., & Bignami, G. F. 2004, Science, 305, 376

De Luca, A., Caraveo, P. E., Mereghetti, S., Negroni, M., & Bignami, G. F. 2004, ApJ, 653, 1051

Fichtel, C. E. et al. 1975, ApJ, 198, 163

Halpern, J. P., & Holt, S. S. 1992, Nature, 357, 222

Halpern, J. P., & Ruderman, M. 1993, ApJ, 415, 286

Halpern, J. P., & Wang, F. Y.-H. 1997, ApJ, 477, 905

Jackson, M. S., Halpern, J. P., Gotthelf, E. V. & Mattox, J. R. 2002 ApJ, 578, 935

Kargaltsev, O. Y., Pavlov, G. G., Zavlin, V. E., & Romani, R. W. 2005, ApJ, in press (astro-ph/0502076)

Mattox, J. R., Halpern, J. P., & Caraveo, P. A. 1998, ApJ, 493, 891

Mattox, J. R., Halpern, J. P., & Caraveo, P. A. 2000, BAAS, 197, #130.05

Shearer, A., et al. 1998, A&A, 335, 21

Thompson, D. J., Fichtel, C. E., Hartman, R. C., Kniffen, D. A., & Lamb, R. C. 1977, ApJ, 213, 252
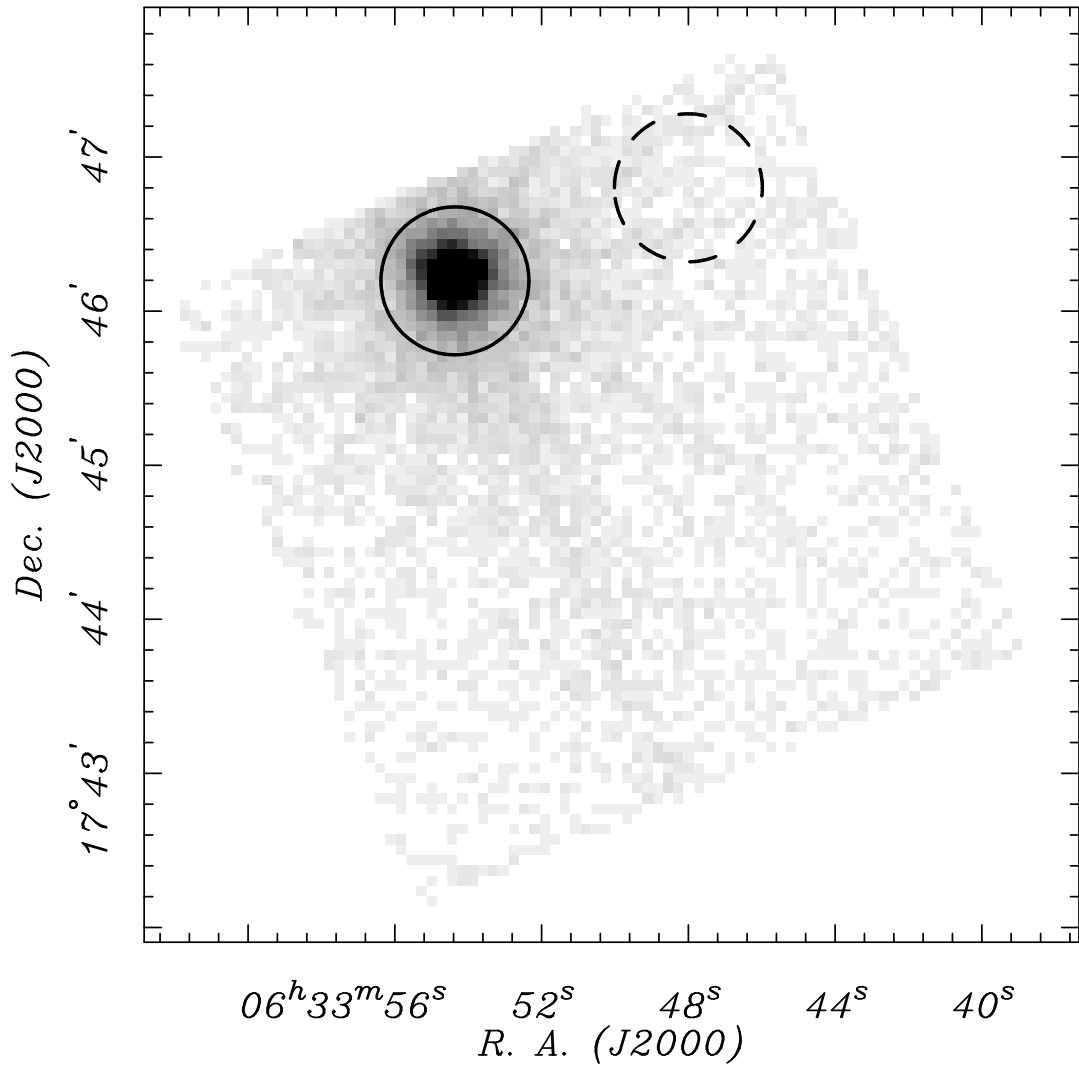
Fig. 1.— *XMM-Newton* pn image of Geminga, showing the source circle (*solid line*) and background circle (*dashed line*) from which the background was subtracted for calculation of the light curves and spectra. The radii of the circles (29″) were chosen to maximize the signal-to-noise ratio in the light curve.
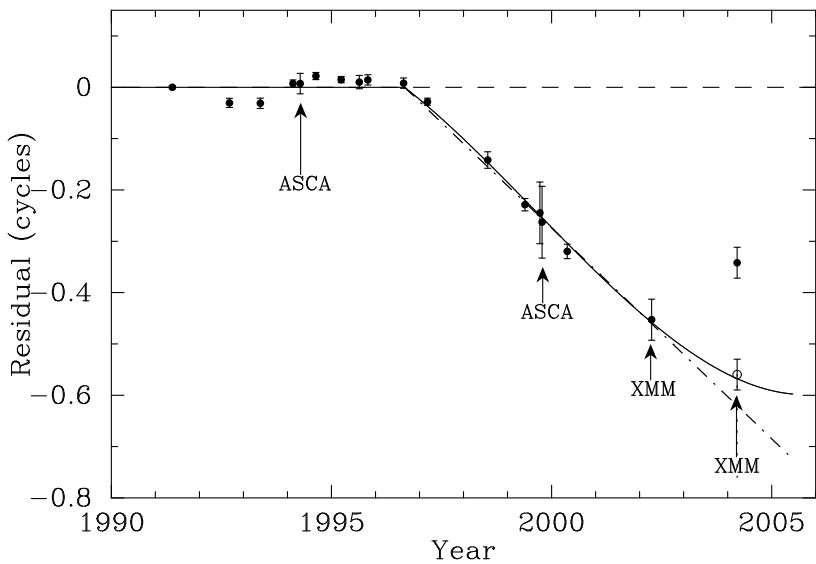
Fig. 2.— Phase residuals of the EGRET timing observations of Geminga relative to the cubic "1997 ephemeris" of Mattox, Halpern, & Caraveo (1998) (pre-glitch ephemeris in Table 2). The 14 unmarked measurements correspond to the numbered EGRET observations in Table 1, some of which were grouped together, and the 1994 and 1999 *ASCA* GIS and 2002 and 2004 *XMM-Newton* pn observations are indicated. The solid line represents the cubic ephemeris segments before and after the glitch. The dash-dot line denotes the previous post-glitch ephemeris given in Jackson et al. (2002), and the dashed line indicates phase zero of the pre-glitch ephemeris. The post-glitch ephemeris is also given in Table 2. The unfilled circle below the 2004 *XMM-Newton* point indicates the phase residual of the data that has been corrected for the possible 1-second error.
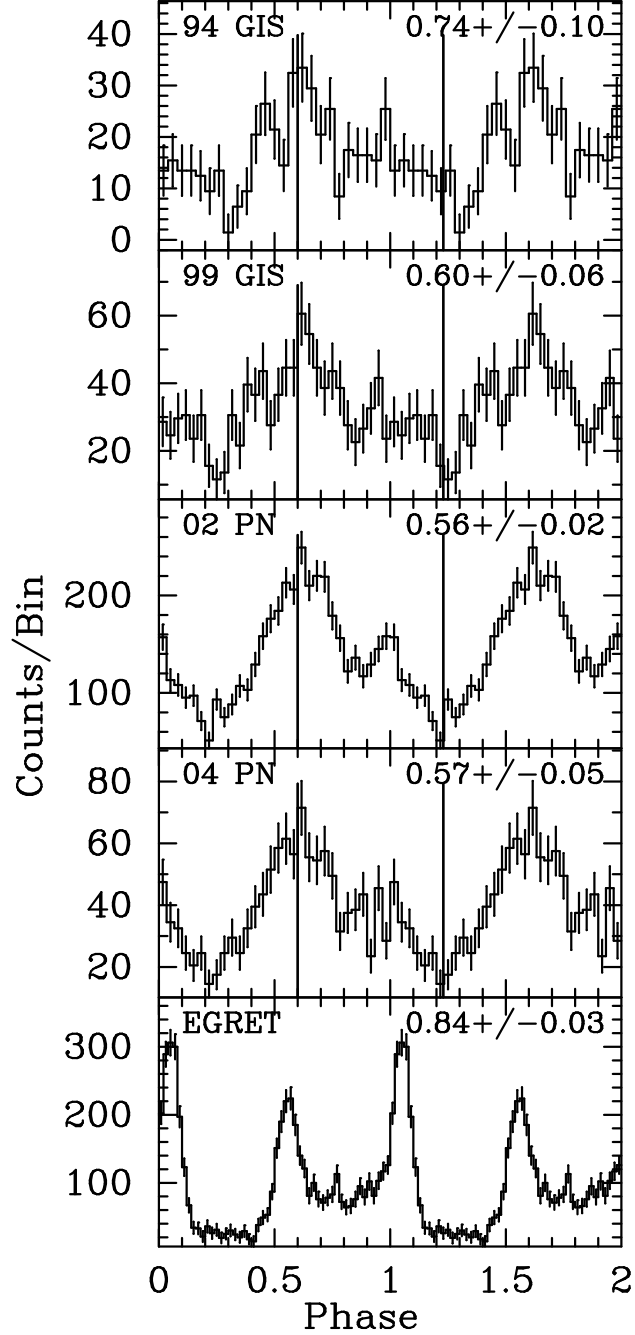
Fig. 3.— Light curves from the four X-ray observations (*ASCA* GIS and *XMM-Newton* pn) at 0.7–2.0 keV, and summed EGRET (*bottom panel*) observations, folded at the applicable ephemeris given in Table 2. The pulsed fraction for the light curves are shown in each panel. The vertical lines show how the peaks and troughs line up from light curve to light curve.
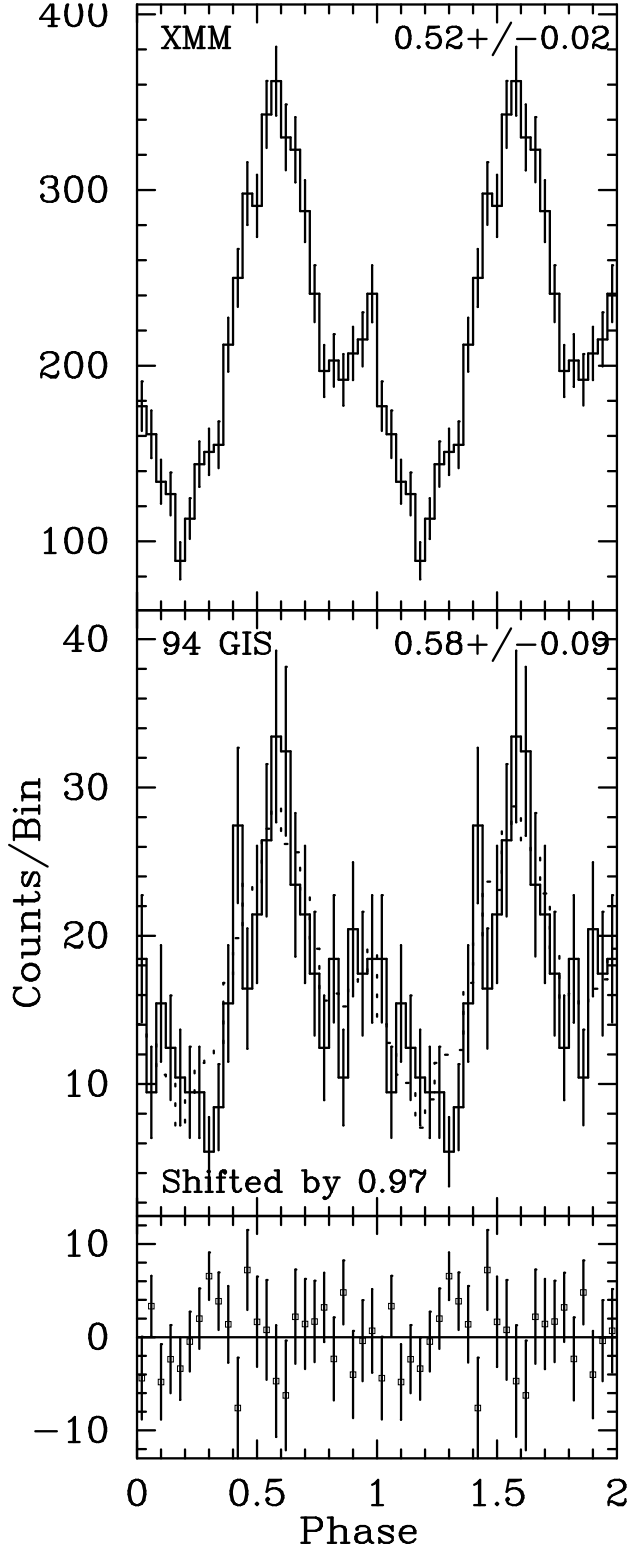
Fig. 4.— A comparison of the 1994 *ASCA* GIS light curve (*middle panel*) and XMM composite light curve (*top panel*) at 0.7–2.0 keV. The lower light curve is shifted in phase by the amount indicated in the lower left corner to best match the upper light curve. The dotted line shows the top light curve normalized to the bottom. The pulsed fractions are indicated in the upper right corner of the panels and the residuals are shown in the bottom panel.
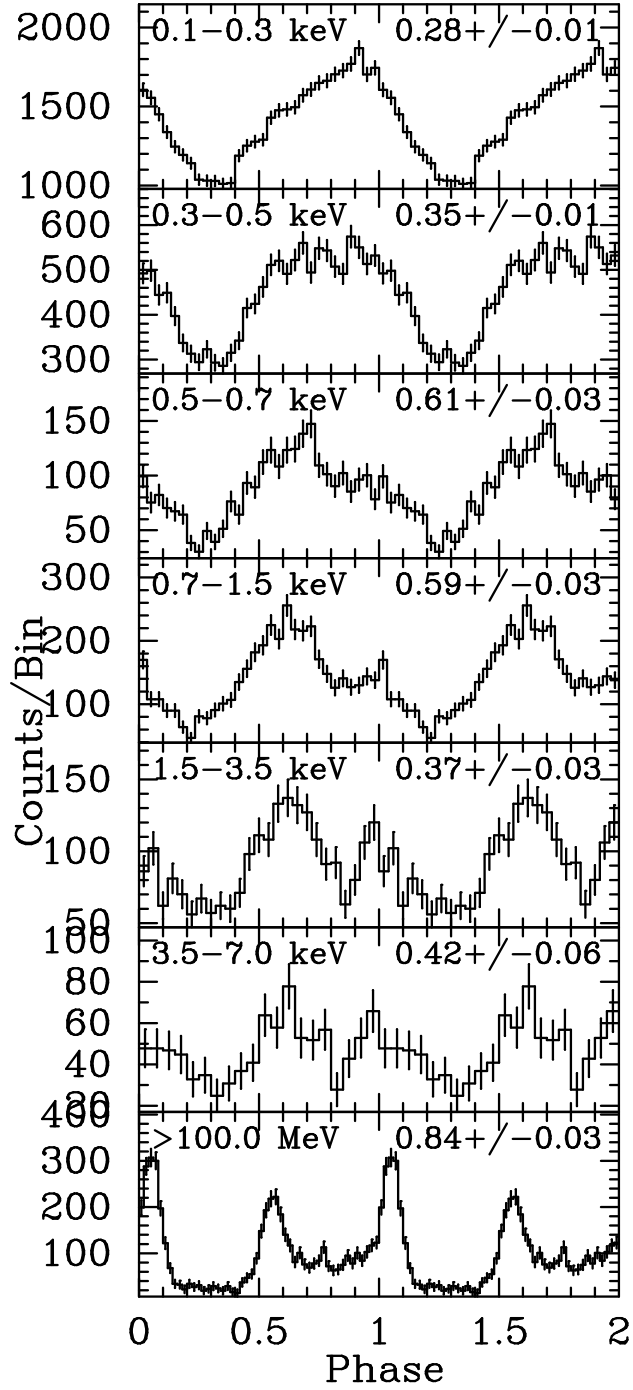
Fig. 5.— Light curves from the summed 2002 and 2004 *XMM-Newton* pn (*top six panels*), and summed EGRET (*bottom panel*) observations, folded at the updated post-glitch ephemeris given in the second column of Table 2. The energy range and pulsed fraction for the light curves are shown in each panel.
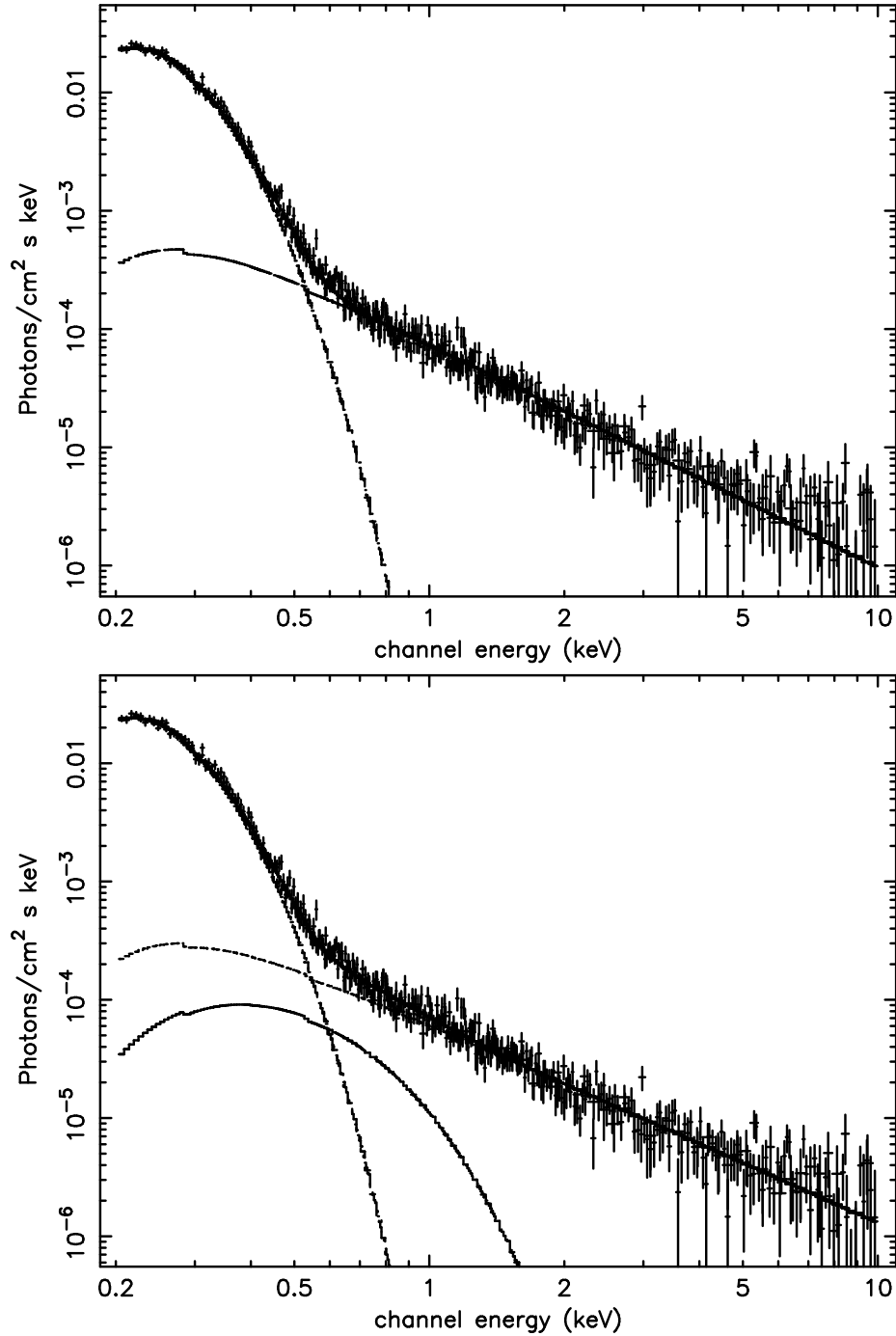
Fig. 6.— Fit of combined *XMM-Newton* pn unfolded spectra of Geminga to *Top panel:* an absorbed power law plus single blackbody (Model A in text); *Bottom panel:* an absorbed power law plus warm and hot blackbody components (Model B in text). The power law and blackbody components are shown in addition to the data and total model. The fitted parameters are given in Table 3.
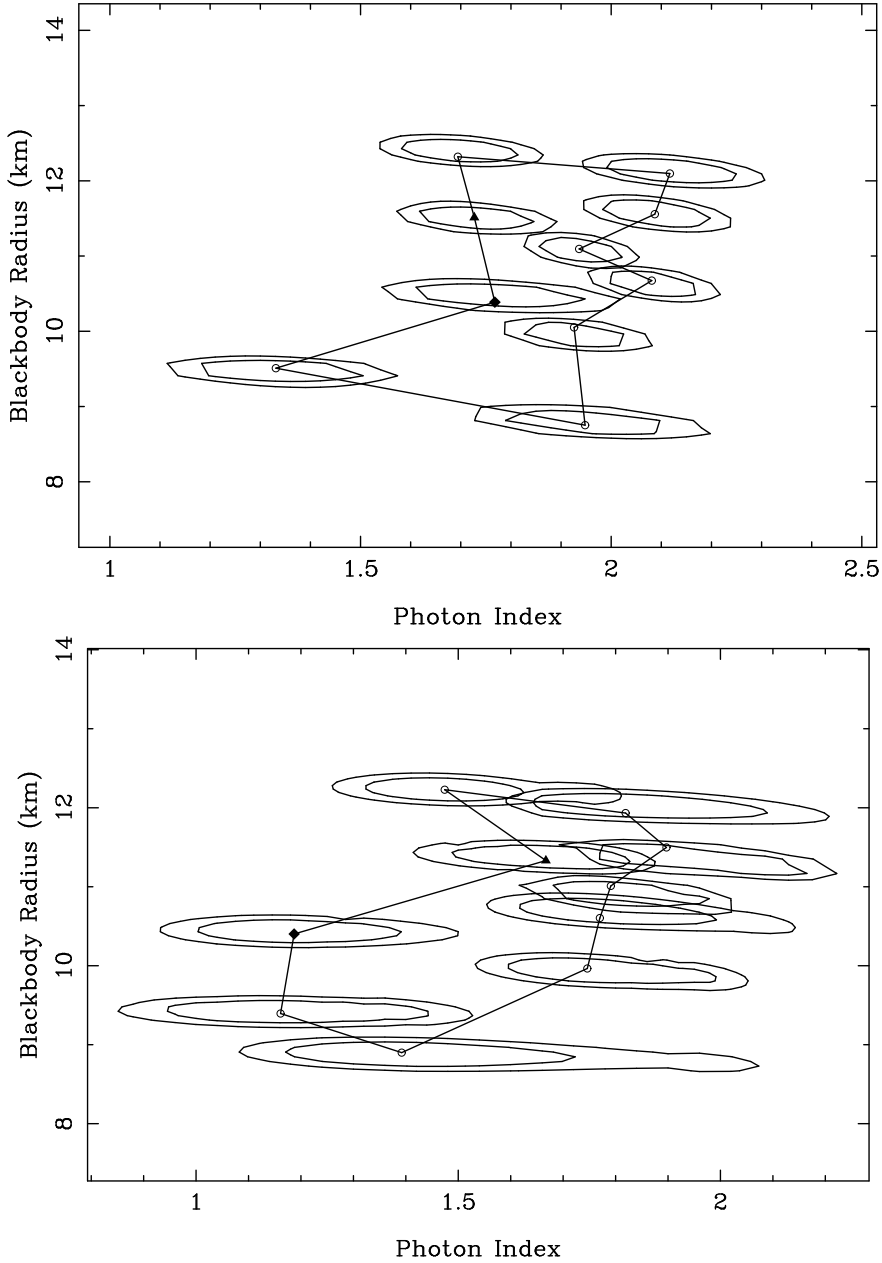
Fig. 7.— Contours of the photon index vs. normalization of the primary (warm) blackbody component. The contours are at 2 and 3 σ for two interesting parameters. The point corresponding to phase 0.0–0.1 is shown as a triangle and the diamond indicates phase 0.1–0.2, with the adjacent phases connected. The top panel shows the contours for the single blackbody model (Model A) and the bottom panel shows the contours for the two blackbody model (Model B).
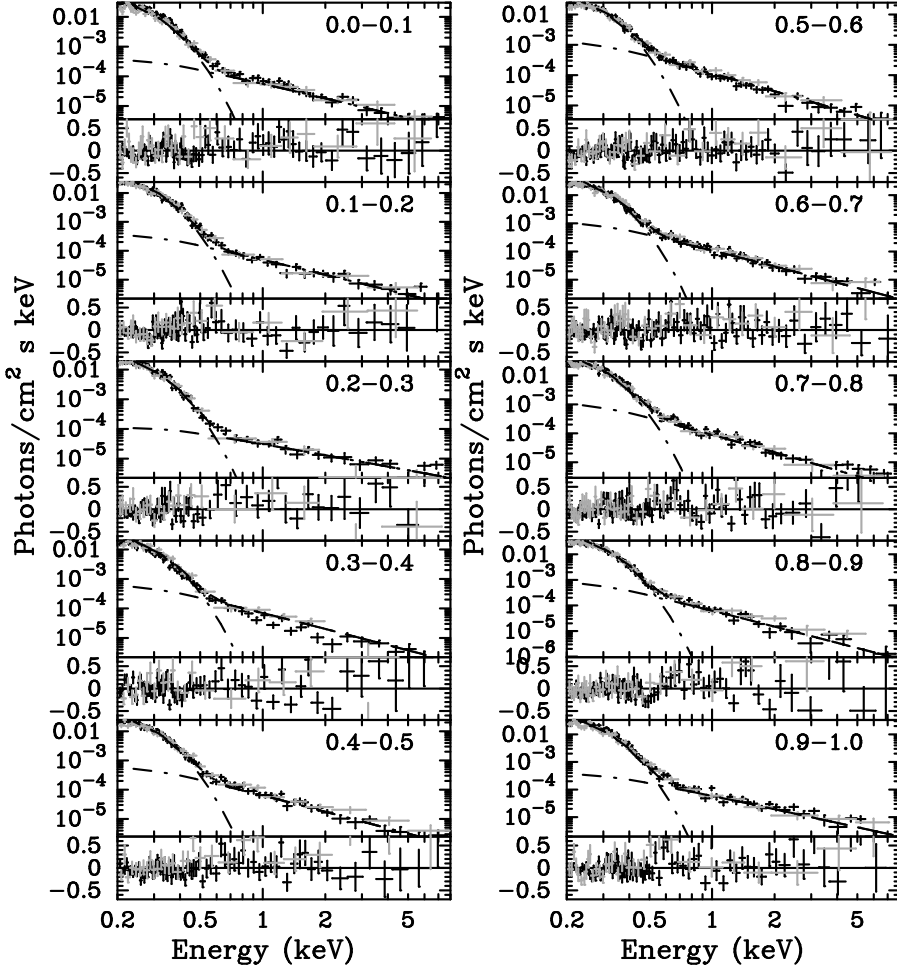
Fig. 8.— Fits of *XMM-Newton* pn phase-resolved spectra to an absorbed power law plus single blackbody (Model A), for phase ranges indicated in the upper corner of each spectrum. The black points correspond to the 2002 observation and the light grey points correspond to the 2004 observation. The fitted parameters are given in Table 4. The power law and blackbody components are shown with the spectra, as well as the total model. The fractional differences between the data and the model are shown below the spectra.
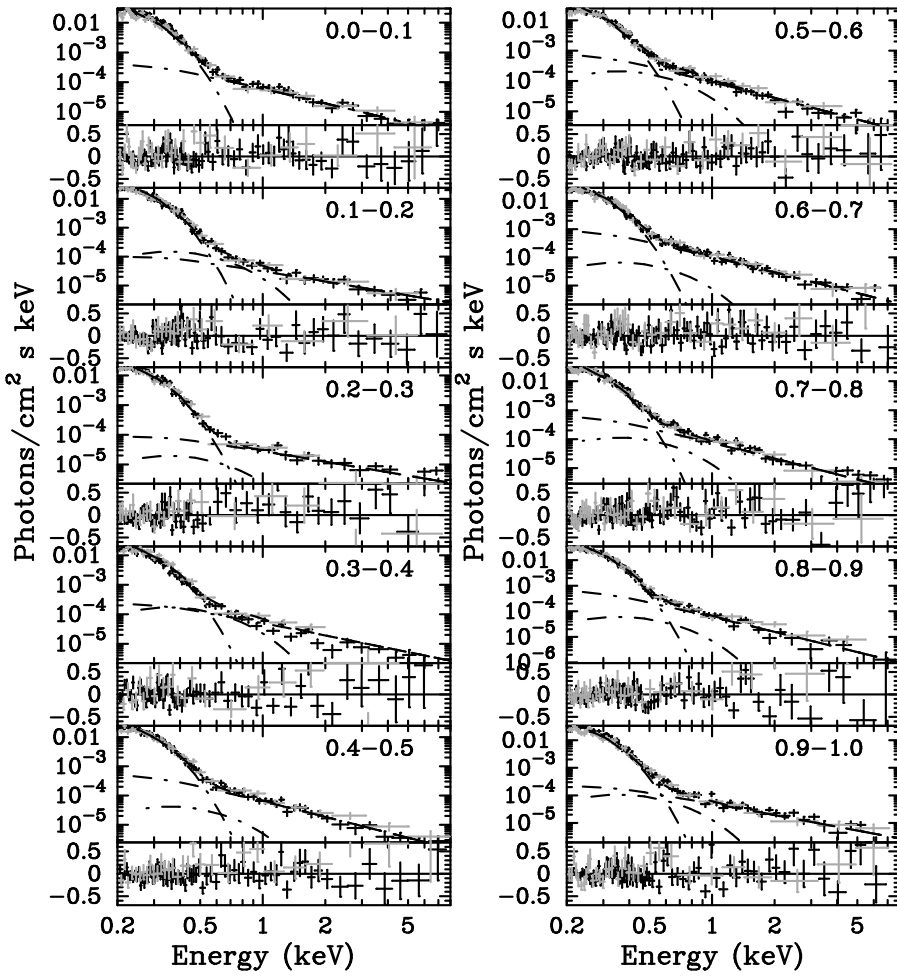
Fig. 9.— Same as Figure 8, for an absorbed power law plus warm and hot blackbody components (Model B).
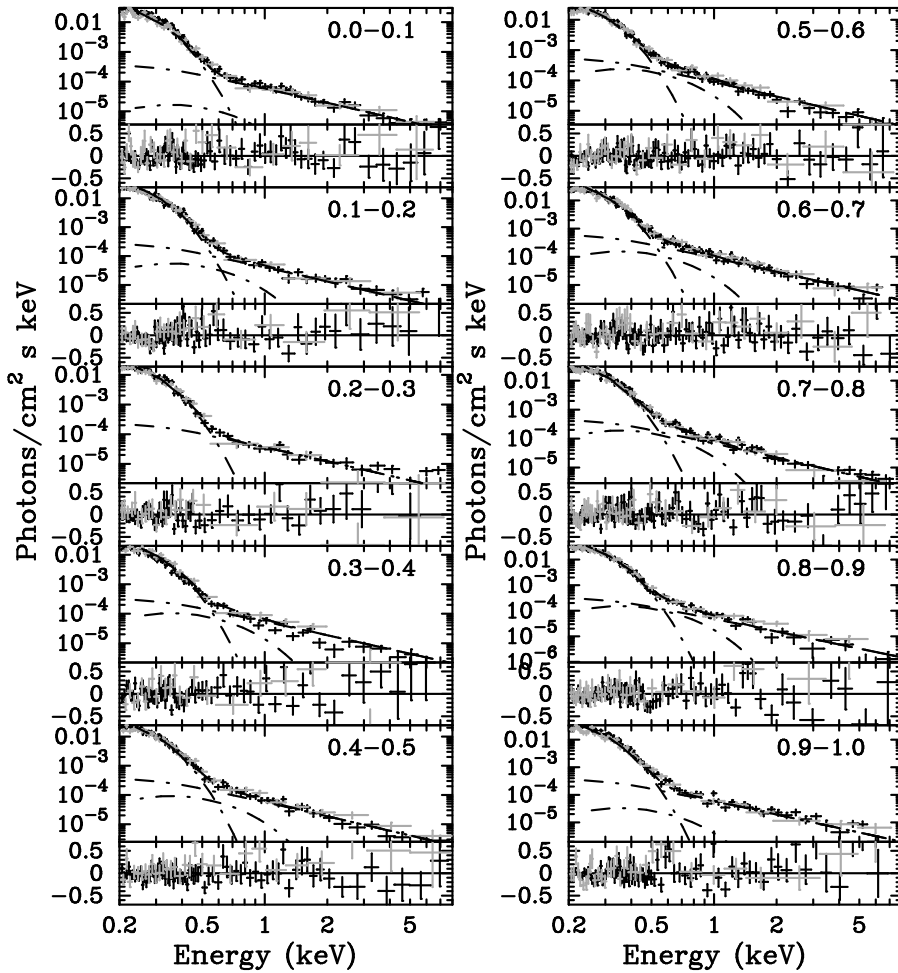
Fig. 10.— Same as Figure 9, with a fixed photon index (Model C).
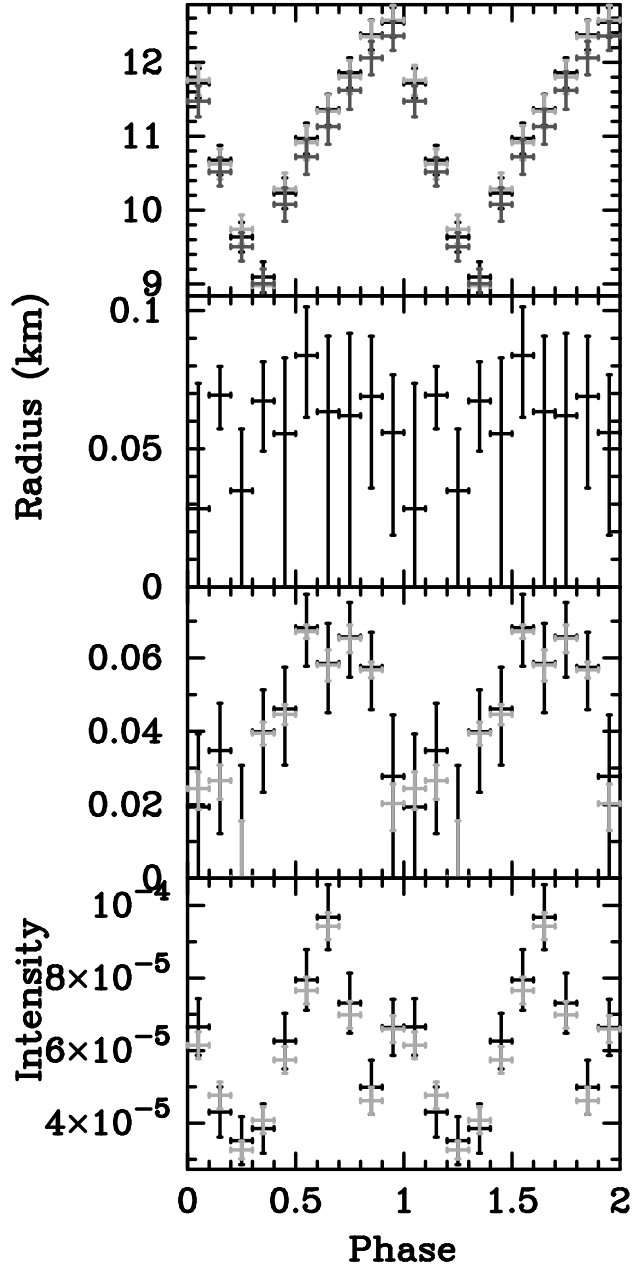
Fig. 11.— Light curves for the modulation of individual spectral components. The top panel shows the modulation of the warm blackbody emitting radius for Models A (*light grey*), B (*dark grey*), and C (*black*). The second panel shows the modulation of the hot blackbody emitting radius for Model B. The third panel shows the hot blackbody emitting radius for Model C (*black*) and fake data (*light grey*). The the bottom panel shows the modulation of the power law for Model C (*black*) and the fake data (*light grey*).

Table 1.   Log of Observations

Instrument	Dates	Exposure time (ks)	Count rate (s^{-1})
EGRET (1)	1991 Apr 22–May 7	1209.6	1.8×10^{-3}
EGRET (1)	1991 May 16–30	1209.6	1.6×10^{-3}
EGRET (1)	1991 Jun 8–15	604.8	1.5×10^{-3}
EGRET (2)	1992 Jun 11–25	1209.6	2.2×10^{-4}
EGRET (2)	1992 Aug 11–20	777.6	1.9×10^{-4}
EGRET (2)	1992 Sep 1–17	1382.4	1.7×10^{-4}
EGRET (2)	1992 Oct 8–15	604.8	1.4×10^{-4}
EGRET (2)	1992 Nov 3–17	1209.6	1.0×10^{-4}
EGRET (3)	1993 Mar 23–29	604.8	3.2×10^{-4}
EGRET (3)	1993 May 13–24	950.4	4.1×10^{-4}
EGRET (4)	1993 Dec 1–13	1036.8	3.5×10^{-4}
EGRET (4)	1994 Feb 8–17	777.6	7.7×10^{-4}
EGRET (5)	1994 Aug 9–29	1814.4	3.7×10^{-4}
EGRET (6)	1995 Feb 28–Mar 21	1814.4	4.0×10^{-4}
EGRET (6)	1995 Apr 4–11	604.8	2.5×10^{-4}
EGRET (6)	1995 May 9–Jun 6	2419.2	1.8×10^{-4}
EGRET (7)	1995 Aug 8–22	1209.6	2.4×10^{-4}
EGRET (8)	1995 Oct 17–31	1209.6	2.7×10^{-4}
EGRET (9)	1996 Jul 30–Aug 27	2419.2	3.4×10^{-4}
EGRET (10)	1997 Feb 18–Mar 18	2419.2	1.5×10^{-4}
EGRET (11)	1998 Jul 7–21	1209.6	2.0×10^{-4}
EGRET (12)	1999 May 11–25	1209.6	2.1×10^{-4}
EGRET (13)	1999 Sep 14–28	1209.6	4.7×10^{-5}
EGRET (14)	2000 Apr 25–May 9	1209.6	2.6×10^{-4}
ASCA SIS	1994 Mar 28–31	49.2	1.7×10^{-2}
ASCA GIS	1994 Mar 28–31	75.3	1.2×10^{-2}
ASCA SIS	1999 Oct 5–11	194.0	1.4×10^{-2}
ASCA GIS	1999 Oct 5–11	207.8	1.0×10^{-2}
XMM pn	2002 Apr 4–5	71.4	0.67
XMM MOS 1	2002 Apr 4–5	101.9	0.12
XMM MOS 2	2002 Apr 4–5	101.9	0.12
XMM pn	2004 Mar 13	18.0	0.71
XMM MOS 1	2004 Mar 13	26.0	0.15
XMM MOS 2	2004 Mar 13	26.0	0.16

Table 2.   The Geminga EGRET Ephemeris

Parameter	Pre-glitch[a]	Post-glitch
Epoch of ephemeris T_0 (MJD)[b]	46599.5	50497.718748124877
Range of valid dates (MJD)	$41725 - 50320$	$50320 - 53078$[c]
Frequency f (Hz)	4.217705363081(13)	4.217639623538(35)
Frequency derivative $\dot{f}$ (Hz s^{-1})	$-1.9521712(12) \times 10^{-13}$	$-1.9515522(81) \times 10^{-13}$
Frequency second derivative $\ddot{f}$ (Hz s^{-2})	$1.49(3) \times 10^{-25}$	0

Parameter[d]	Value
Epoch of position (MJD)	49793.5
R.A. (J2000)	$6^{\mathrm{h}}33^{\mathrm{m}}54\fs153$
Decl. (J2000)	$+17°46'12\farcs91$
R.A. proper motion μ_α (mas yr^{-1})	138
Decl. proper motion μ_δ (mas yr^{-1})	97

[a]From Mattox, Halpern, & Caraveo (1998).

[b]Epoch of phase zero in all light curves

[c]The post-glitch ephemeris is provisional after the 2002 observation (MJD 52369), depending upon whether a glitch occured between then and the 2004 observation.

[d]Position and proper motion from Caraveo et al. (1998).

Note. — Digits in parentheses following a parameter value indicate ∼95% confidence uncertainties in the last digits of the parameter.

Table 3.   Fits to XMM pn Spectra

Parameter	1 Blackbody		2 Blackbody	
	2002 Observation	2002+2004 Combined	2002 Observation	2002+2004 Combined
n_{H} (10^{20}cm^{-2})	1.75 ± 0.63	1.75 ± 0.56	1.76 ± 1.11	1.76 ± 0.95
Γ	1.901 ± 0.038	1.895 ± 0.034	1.697 ± 0.067	1.684 ± 0.060
PL Normalization[a]	7.44 ± 0.39	7.56 ± 0.35	6.22 ± 0.85	6.30 ± 0.76
T_{w} (10^5 K)	4.804 ± 0.015	4.818 ± 0.013	4.773 ± 0.022	4.800 ± 0.020
R_{w} (km)	11.0424 ± 1.46	11.0297 ± 1.11	11.35 ± 0.87	11.17 ± 1.09
T_{h} (10^5 K)	$\cdots$	$\cdots$	17.0 ± 2.6	17.1 ± 2.3
R_{h} (m)	$\cdots$	$\cdots$	$62. \pm 39.$	$62. \pm 34.$
Reduced χ^2	1.189 (316 dof)	1.208 (468 dof)	1.131 (314 dof)	1.165 (466 dof)

[a]10^{-5} photons keV^{-1}cm^{-2}s^{-1} at 1 keV

Table 4.   Fits to XMM pn Phase Resolved Spectra.

Phase	Model	Γ	PL Normalization at 1 keV $(10^{-5}$ photons keV^{-1}cm^{-2}s$^{-1})$	$T_{\rm w}$ $(10^5$ K)	$R_{\rm w}$ (km)	$T_{\rm h}$ $(10^5$ K)	$R_{\rm h}$ (m)	Reduced χ^2 (dof)
0.0–0.1	A	1.727 ± 0.068	6.42 ± 0.59	(4.818)	11.37 ± 0.35	$\cdots$	$\cdots$	1.128 (110)
	B	1.667 ± 0.183	6.92 ± 1.83	(4.800)	11.37 ± 0.36	(17.1)	$0. \pm 71.$	1.106 (109)
	C	(1.684)	6.65 ± 0.78	(4.800)	11.72 ± 0.20	(17.1)	$19. \pm 20.$	1.097 (110)
0.1–0.2	A	1.768 ± 0.101	5.14 ± 0.51	(4.818)	10.20 ± 0.32	$\cdots$	$\cdots$	1.129 (95)
	B	1.187 ± 0.195	3.27 ± 0.99	(4.800)	10.44 ± 0.32	(17.1)	$79. \pm 15.$	1.074 (94)
	C	(1.684)	4.30 ± 0.69	(4.800)	10.68 ± 0.20	(17.1)	$35. \pm 13.$	1.089 (95)
0.2–0.3	A	1.331 ± 0.092	2.94 ± 0.47	(4.818)	9.37 ± 0.28	$\cdots$	$\cdots$	1.373 (83)
	B	1.161 ± 0.196	2.64 ± 0.97	(4.800)	9.43 ± 0.29	(17.1)	$27. \pm 30.$	1.156 (82)
	C	(1.684)	3.52 ± 0.66	(4.800)	9.64 ± 0.20	(17.1)	$0. \pm 31.$	1.213 (83)
0.3–0.4	A	1.948 ± 0.114	5.04 ± 0.50	(4.818)	8.61 ± 0.31	$\cdots$	$\cdots$	1.379 (82)
	B	1.392 ± 0.268	3.53 ± 1.32	(4.800)	8.93 ± 0.28	(17.1)	$71. \pm 22.$	1.377 (81)
	C	(1.684)	3.85 ± 0.68	(4.800)	9.09 ± 0.21	(17.1)	$40. \pm 11.$	1.325 (82)
0.4–0.5	A	1.926 ± 0.066	6.97 ± 0.59	(4.818)	9.91 ± 0.33	$\cdots$	$\cdots$	0.952 (102)
	B	1.746 ± 0.184	6.96 ± 1.92	(4.800)	10.00 ± 0.33	(17.1)	$42. \pm 43.$	0.893 (101)
	C	(1.684)	6.26 ± 0.77	(4.800)	10.23 ± 0.21	(17.1)	$46. \pm 11.$	0.892 (102)
0.5–0.6	A	2.081 ± 0.059	10.04 ± 0.67	(4.818)	10.53 ± 0.38	$\cdots$	$\cdots$	0.928 (120)
	B	1.770 ± 0.182	8.47 ± 2.26	(4.800)	10.64 ± 0.39	(17.1)	$88. \pm 32.$	0.930 (119)
	C	(1.684)	7.95 ± 0.84	(4.800)	10.97 ± 0.21	(17.1)	$68. \pm 9.$	0.911 (120)
0.6–0.7	A	1.936 ± 0.052	11.52 ± 0.71	(4.818)	10.95 ± 0.39	$\cdots$	$\cdots$	1.117 (131)
	B	1.791 ± 0.141	10.85 ± 2.30	(4.800)	11.05 ± 0.40	(17.1)	$52. \pm 44.$	1.108 (130)
	C	(1.684)	9.68 ± 0.90	(4.800)	11.36 ± 0.21	(17.1)	$59. \pm 11.$	1.114 (131)
0.7–0.8	A	2.087 ± 0.063	9.59 ± 0.66	(4.818)	11.42 ± 0.41	$\cdots$	$\cdots$	1.260 (123)
	B	1.897 ± 0.184	7.95 ± 2.15	(4.800)	11.53 ± 0.40	(17.1)	$69. \pm 36.$	1.274 (122)
	C	(1.684)	7.31 ± 0.83	(4.800)	11.86 ± 0.20	(17.1)	$66. \pm 9.$	1.242 (123)
0.8–0.9	A	2.117 ± 0.080	6.53 ± 0.59	(4.818)	11.96 ± 0.42	$\cdots$	$\cdots$	1.203 (111)
	B	1.819 ± 0.270	6.32 ± 2.20	(4.800)	11.97 ± 0.42	(17.1)	$50. \pm 46.$	1.165 (110)
	C	(1.684)	4.99 ± 0.75	(4.800)	12.37 ± 0.20	(17.1)	$57. \pm 10.$	1.182 (111)
0.9–1.0	A	1.694 ± 0.070	6.72 ± 0.59	(4.818)	12.18 ± 0.39	$\cdots$	$\cdots$	1.317 (112)
	B	1.474 ± 0.156	5.67 ± 1.35	(4.800)	12.27 ± 0.19	(17.1)	$69. \pm 23.$	1.293 (111)
	C	(1.684)	6.64 ± 0.77	(4.800)	12.54 ± 0.20	(17.1)	$28. \pm 17.$	1.298 (112)

Note. — Values in parentheses are parameters that were frozen for the fits.